Volume 205 September 2013 ISSN 0022-4596

ELSEVIER

JOURNAL OF SOLID STATE CHEMISTRY

IN THIS ISSUE:

4,4′-Bipyridine-aided synthesis and characterization of Zn(II) and Cd(II) 2-sulfoterephthalate complexes

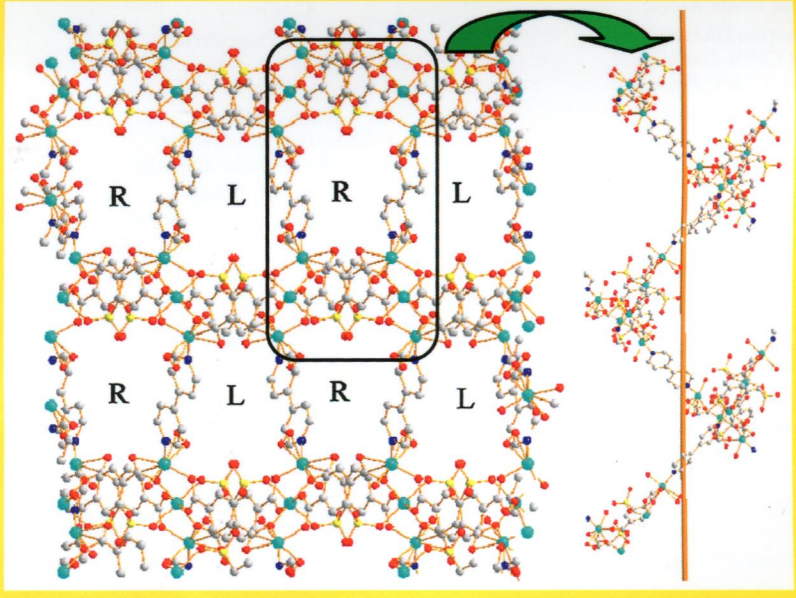

Shan-Shan Xiao, Xin-Xin Li, Xiang-Jun Zheng, Tian-Jing Jia and Lin-Pei Jin

ELSEVIER

Volume 205, September 2013

CONTENTS

JOURNAL OF SOLID STATE CHEMISTRY

www.elsevier.com/locate/jssc

Abstracted/indexed in BioEngineering Abstracts, Chemical Abstracts, Coal Abstracts, Current Contents/Physics, Chemical, & Earth Sciences, Engineering Index, Research Alert, SCISEARCH, Science Abstracts, and Science Citation Index. Also covered in the abstract and citation database SciVerse SCOPUS®. Full text available on SciVerse ScienceDirect®.

Regular Articles

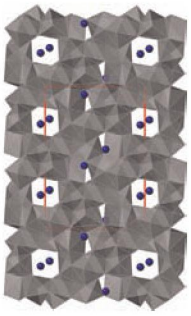

Structure of $Rb_2Th_7Se_{15}$ viewed down the *b*-axis.

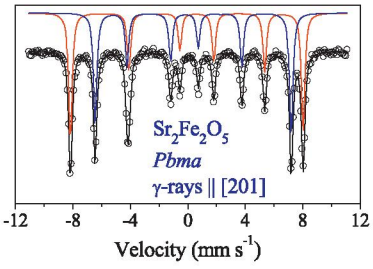

Mössbauer spectra of powdered and oriented single-crystal $Sr_2Fe_2O_5$, analyzed by solving the complete Hamiltonian for hyperfine interactions in the excited and ground states of the ^{57}Fe nuclei, show that the magnetic moments of both octahedrally and tetrahedrally coordinated iron cations are parallel to the shortest *c*-axis of the orthorhombic brownmillerite unit cell.

Regular Articles—Continued

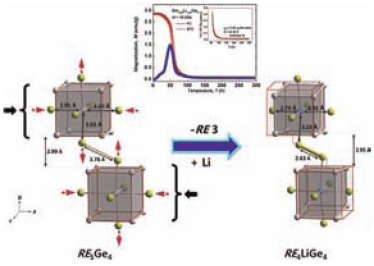

Reported is a combined effect of the chemical pressure and the reduced VEC caused by the smaller monovalent non-magnetic Li substitution for the larger trivalent magnetic rare-earth metals in the RE_4LiGe_4 (*RE*=La, Ce, Pr, and Sm) system. This results in the structure transformation from the Sm_5Ge_4-type to the Gd_5Si_4-type structure and the changes in magnetic properties.

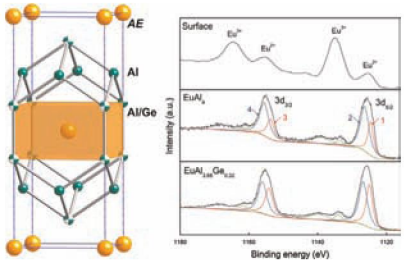

AE$Al_{4-x}Ge_x$ (*AE*=Eu, Sr, Ba; $0.32(1)\leq x\leq0.41(1)$), three "electron-rich" phases with $BaAl_4$ structure type have been synthesized and characterized.

Continued

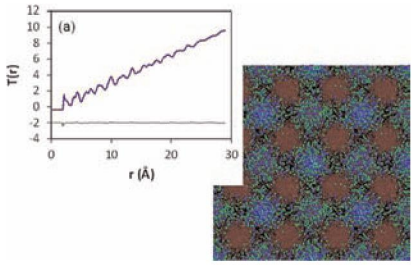

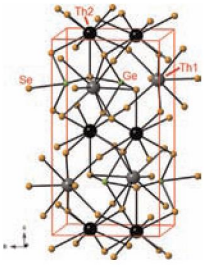

The structure of Th_2GeSe_5.

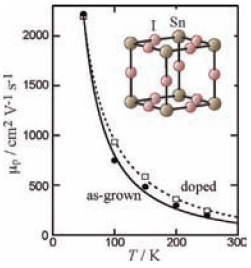

Hall effect measurements of as-grown $CH_3NH_3SnI_3$ crystals give a hole concentration of about 9×10^{17} cm^{-3}. Artificial hole doping enhances the electrical conductivity of the crystals without influencing mobility, indicating that the electronic structure of $CH_3NH_3SnI_3$ can be described as that of an intrinsic semiconductor with a wide valence band.

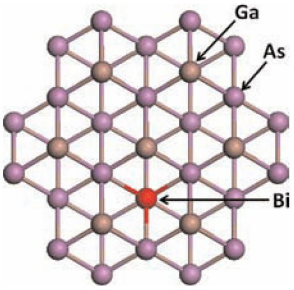

Top view of Bi-doped GaAs nanowires. Ga, As, and Bi atoms are denoted with grey, purple and red balls, respectively.

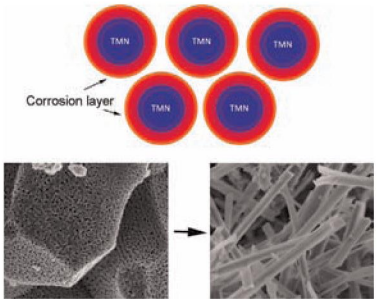

Corrosion behavior of mesoporous transition metal nitrides (*TM*=Nb, V, Cr and Ti) in acidic and alkaline solutions at 80 °C for 2 weeks.

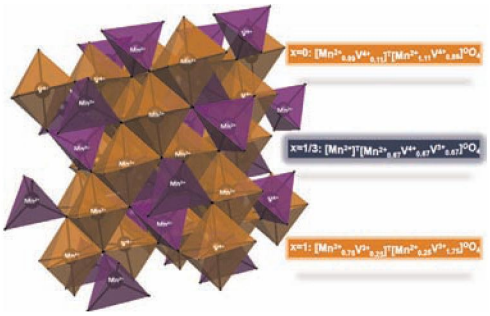

View of the crystallographic structure of a spinel. It shows as an example one of the models of ion distribution determined for the spinels $Mn_{(2-x)}V_{(1+x)}O_4$ (x=0, 1/3,1).

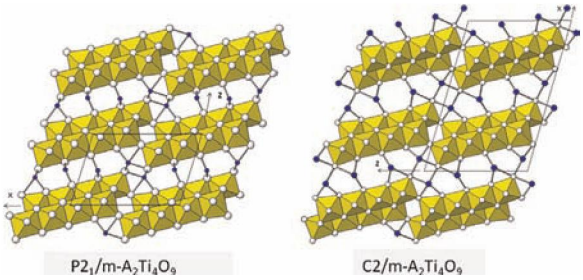

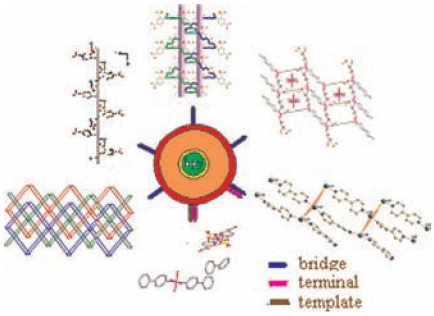

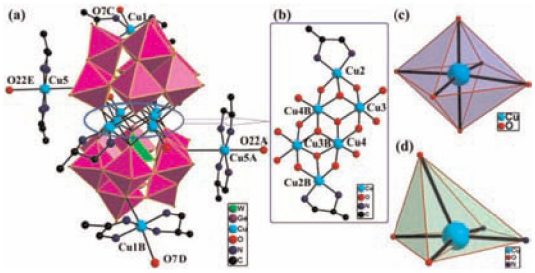

A hexa-Cu^{II} sandwiched germanotungstate has been synthesized and structurally characterized. The magnetic, solid-state electrochemical and electrocatalytic properties have been investigated.

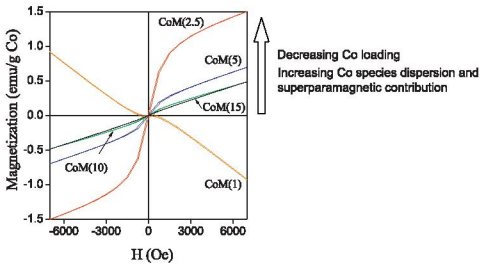

Room temperature hysteresis loops as a function of the Co content.

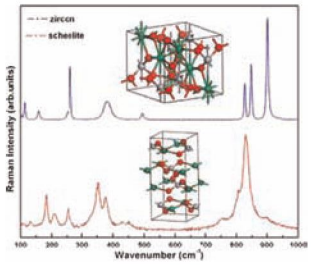

Lutetium orthovanadate polymorphs were synthesized by SSR and HP methods and their physical and chemical properties, including lattice dynamical properties, were determined by DFT calculations and experiments.

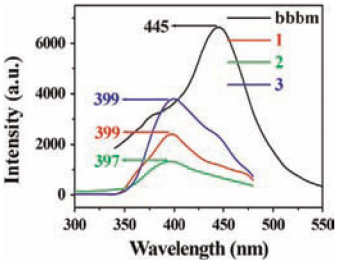

Three bis(benzimidazole)-based cobalt(II) coordination polymers tuned by aromatic carboxylates were hydrothermally synthesized and structurally characterized. The aromatic carboxylates play a key role in the dimensionality of three polymers. The electrochemical and luminescent properties of three polymers were investigated.

Continued

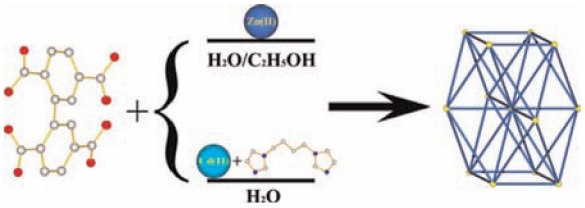

Two new compounds with unusual 12-connected *fcu* topology display intriguing structural feature, as well as luminescence property.

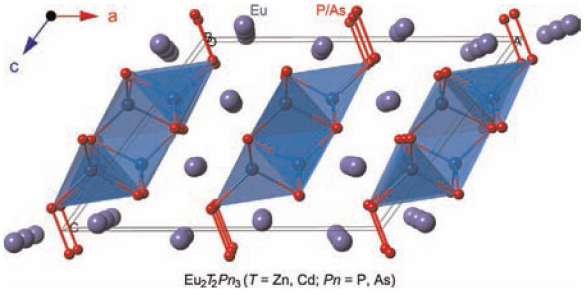

A polyhedral view of the crystal structure of new pnictides $Eu_2T_2Pn_3$ (*T*=Zn or Cd; *Pn*=P or As).

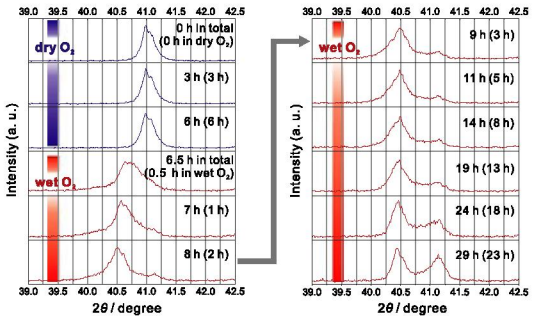

A $BaCe_{0.8}Y_{0.2}O_{3-\delta}$ rhombohedral phase transited to a monoclinic phase at 300 °C when moisture was introduced into the atmosphere.

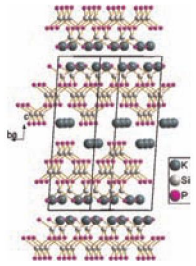

KSi_2P_3 contains two-dimensional layer [Si_2P_3] separated by K^+ cations.

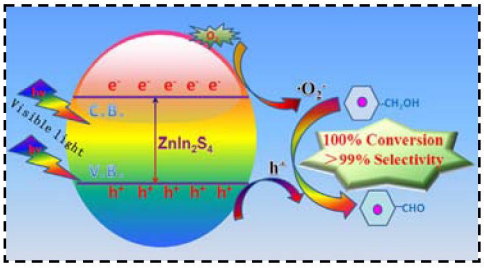

Marigold-like $ZnIn_2S_4$ microspheres were synthesized by a solvothermal method. The high visible photocatalytic activities of $ZnIn_2S_4$ were evaluated by selective oxidation of benzyl alcohol to benzaldehyde under mild conditions.

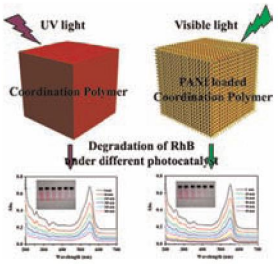

PANI loaded coordination polymer composite material, which displays excellent photocatalytic activity under visible light was firstly synthesized through in-situ chemical oxidation of aniline on surface of coordination polymer.

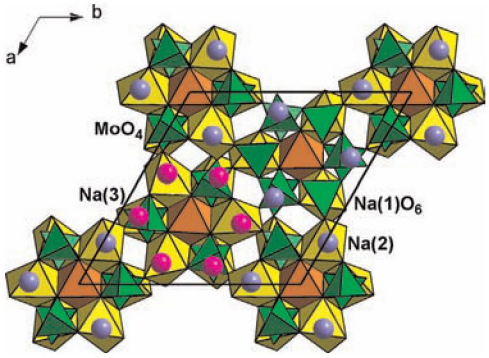

A new double molybdate $Na_9Fe(MoO_4)_6$ was synthesized and structurally characterized, its physicochemical properties were studied.

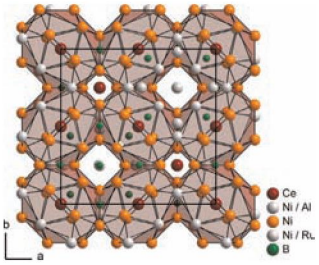

Single crystals of $Ce_3Ni_{25.75}Ru_{3.16}Al_{4.1}B_{10}$ were obtained using a process in which a polycrystalline sample of $CeRu_2Al_2B$ was annealed in an excess of a Ni–In flux. Electrical resistivity measurements reveal metallic behavior with a minimum of 700 μΩ cm and a small residual resistivity ratio of RRR=1.4 indicating a large amount of disorder scattering. The cerium atoms are either in the 4+ or an intermediate valence state with a valence fluctuation temperature far above room temperature.

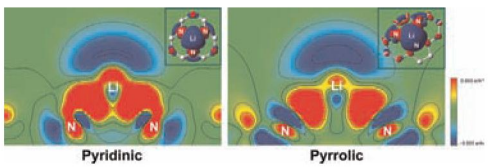

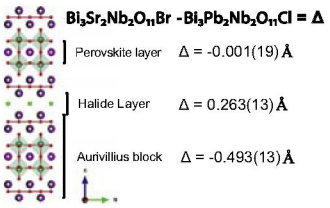

The structural expansion and contractions in the stacking axis of co-doped Sillen–Aurivillius phases.

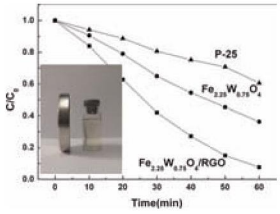

Magnetically recyclable $Fe_{2.25}W_{0.75}O_4$/reduced graphene oxide nanocomposites with enhanced photocatalytic property

---

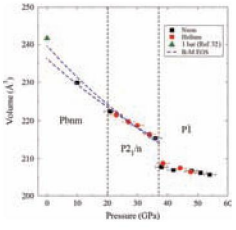

Unit cell volume as a function of pressure (T=6 K). Black squares and red circles correspond to Ne and He pressure media, respectively. Blue dashed lines are fit to the data before the volume collapse using a second-order Birch–Murnaghan equation of state excluding (lower curve) and including (upper curve) neutron diffraction data for the low temperature, ambient pressure volume. Dashed lines denote structural phase boundaries.

Continued

Synthesis, crystal structure and luminescence properties of lanthanide coordination polymers with a new semirigid bridging thenylsalicylamide ligand

Xue-Qin Song, Li Wang, Meng-Meng Zhao, Xiao-Run Wang, Yun-Qiao Peng and Guo-Quan Cheng

page 183

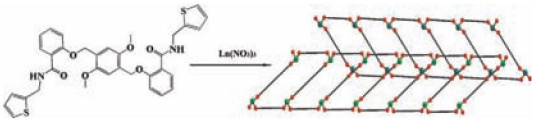

We present herein one dimensional lanthanide coordination polymers of a new semirigid *exo*-bidentate ligand which not only display interesting structures but also possess strong luminescence properties.

Structural investigation of the new $Ca_3Ln_2Ge_3O_{12}$ (*Ln*=Pr, Nd, Sm, Gd and Dy) compounds and luminescence spectroscopy of $Ca_3Gd_2Ge_3O_{12}$ doped with the Eu^{3+} ion

F. Piccinelli, A. Lausi and M. Bettinelli

page 190

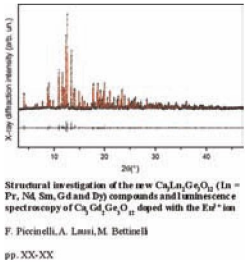

The structural study on $Ca_3Ln_2Ge_3O_{12}$ exploiting synchrotron X-ray diffraction, allows us to determine the detailed geometry of the coordination polyhedra of the metals and their distribution in the crystal sites. These features are, in the case of $Ca_3Gd_2Ge_3O_{12}$ host, closely related to the luminescence spectroscopy of the Eu^{3+} dopant ion.

Defect chemistry of phospho-olivine nanoparticles synthesized by a microwave-assisted solvothermal process

Craig A. Bridges, Katharine L. Harrison, Raymond R. Unocic, Juan-Carlos Idrobo, M. Parans Paranthaman and Arumugam Manthiram

page 197

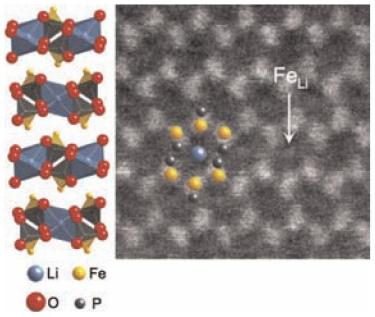

Temperature-dependent antisite defect formation has been observed in nanocrystalline $LiFePO_4$ powders synthesized by a microwave solvothermal process, using high resolution diffraction and STEM imaging.

Syntheses and characterizations of two new energetic copper–amine-DNANT complexes and their effects on thermal decomposition of RDX

Qianqian Qiu, Kangzhen Xu, Shihe Yang, Zhe Gao, Hang Zhang, Jirong Song and Fengqi Zhao

page 205

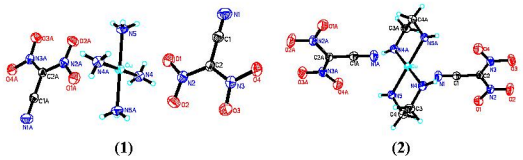

$Cu(NH_3)_4(DNANT)_2$ (**1**) and $Cu(en)_2(DNATN)_2$ (**2**) have been first synthesized through an unique reaction. Cu^{2+} ion shares a similar four-coordinated structure in the two complexes.

Functionalized mesoporous silica materials for molsidomine adsorption: Thermodynamic study

Nonna A. Alyoshina and Elena V. Parfenyuk

page 211

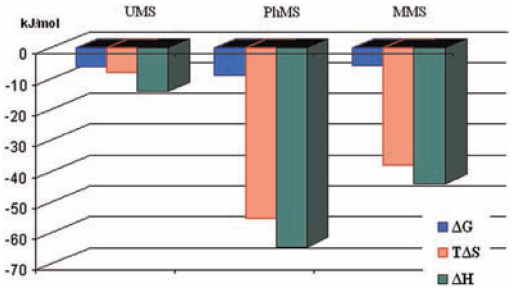

Comparative analysis of the thermodynamic characteristics of molsidomine adsorption showed that the adsorption process on mesoporous silica materials is controlled by chemical nature of surface functional groups. Molsidomine adsorption on the phenyl modified silica is the most quantitatively and energetically favorable. Taking into account ambiguous nature of mesoionic compounds, it was found that molsidomine is rather aromatic than dipolar.

Structural stability of ternary *C*22–Zr_6X_2Co (*X*=Al, Ga, Sn, As, Sb, Bi, Te) and *C*22–Zr_6Sn_2T' (*T'*=Fe, Co, Ni, Cu) compounds

Catherine Colinet, Jean-Claude Crivello and Jean-Claude Tedenac

page 217

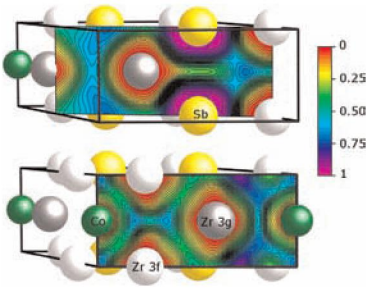

Valence charge electronic localization function (ELF) calculated for Zr_6Sb_2Co compound.

Lifting the geometric frustration through a monoclinic distortion in "114" $YBaFe_4O_{7.0}$: Magnetism and transport
V. Duffort, T. Sarkar, V. Caignaert, V. Pralong, B. Raveau, M. Avdeev, A. Cervellino, J.C. Waerenborgh and E.V. Tsipis
page 225

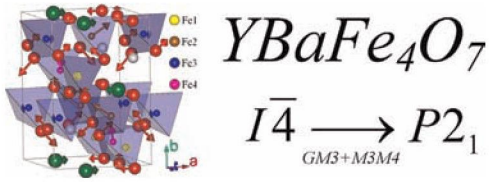

Atomic displacements at the tetragonal-monoclinic transition in $YBaFe_4O_7$.